

A Reconfigurable Perovskite/Polymer Composite Film for Real-Time Detection of Agricultural Spraying

Haoran Zhang

The Chinese University of Hong Kong, Shenzhen

Xubing Wu

Zhejiang University

Jiaying Du

The Chinese University of Hong Kong, Shenzhen

Song Wang

Zhejiang University

Hui Fang

Zhejiang University

Qi Zhang

The Chinese University of Hong Kong, Shenzhen

Wen-Jun Wang

Zhejiang University

Shiping Zhu

The Chinese University of Hong Kong, Shenzhen

Johan Hofkens

KU Leuven

Pingwei Liu (✉ liupingwei@zju.edu.cn)

Zhejiang University

Article

Keywords: perovskite/polymer composite film, polymer network mesh, agriculture

Posted Date: August 20th, 2021

DOI: <https://doi.org/10.21203/rs.3.rs-754328/v1>

License:   This work is licensed under a Creative Commons Attribution 4.0 International License.

[Read Full License](#)

Abstract

Responsive composites that can display sophisticated responses under environmental stimuli are of paramount importance for developing smart materials and systems. However, the hierarchical design of their multiscale constituents to achieve such response remains a challenge. Here, we report a responsive polymer composite obtained by integrating hierarchical interactions between the polymer network meshes, perovskite nanoinclusion, and a microstructured layout. More specific, a layered composite film has been made with perovskite nanoparticles embedded in a hydratable polymer network as the top layer. The perovskites inclusions can undergo a reversible transformation between a nanocrystalline state and a dissociated ion state, triggered by spraying aqueous solutions on the polymer top layer, resulting in an on/off switch of fluorescence at 510 nm. Meanwhile, the surface layer experiences a reconfigurable micro-wrinkling that can gradually change the film transmittance between 90% and 10%. The two orthogonal responses show a good reversibility for at least 15 cycles. They can be manipulated independently as they respond differently to the amount of water applied. We demonstrate the use of such film by real-time, quantitative, and repeatable detection of spraying and subsequent droplet distribution. Such a sensing capability is urgently needed in precision agriculture for fast assessing the deposition quality of pesticides and fertilizers, yet still not available. Our findings enable the design of perovskite-based responsive composites with multiple functions as well as novel device applications in sensors, actuators, and optoelectronics.

Main Text

Reconfigurable materials with multi-functionality and reversibility^{1,2} are crucial for the development of sensors³, actuators^{4,5}, wearable devices^{6,7}, and soft robotics⁸⁻¹⁰. A number of such materials with specific functionality or responsiveness were obtained via the hybridization of polymer matrices with inorganic inclusions such as nano-sized carbons¹¹⁻¹³, metals^{14,15}, metal oxides¹⁶, and others¹⁷⁻¹⁹. Versatility of the composite can be engineered via a multi-scale design at different levels, ranging from the constituting polymer chain²⁰⁻²² to microstructured features^{23,24}. In designing them, a critical issue would be how to achieve hierarchical interactions between the multiscale constituents so that they can address synergistically complex tasks²⁵. This is challenging, given that the bespoke nano-inclusions usually maintain good physicochemical stability with limited reversibility or reconfigurability in the polymer support.

Solution processable perovskites may provide new opportunities for the hierarchical design of responsive polymer composites with complex functions. Perovskites are widely used in photovoltaics^{26,27}, light-emitting diodes²⁸⁻³¹, display³², and photodetectors³³ with long carrier lifetime, high carrier mobility, and high fluorescence quantum yield. However, as ionic solids, they are highly sensitive to water, *i.e.*, water can induce (ir)reversible phase change³⁴⁻³⁶ or even dissociation of the perovskite crystal³⁷⁻⁴⁰. Tremendous efforts have been devoted to improving their stability against water, for example by using hydrophobic passivation^{41,42} and encapsulation⁴³⁻⁴⁵. Here, we ask ourselves if this inherent instability

can be utilized and manipulated with a hydrophilic and hydratable polymer network, leading to novel responsive polymer composites with hierarchical synergies and exotic functionalities capable of complex device operations.

We first designed the structure and fabrication scheme of a multi-layered and perovskite-embedded composite film (Fig. 1a, also see details in “Methods” and Figure S1). A polymeric three-layer film was constructed via stepwise spin-coating (Fig. 1a, left). The top layer is a water-absorbing polyvinyl alcohol (PVA) film that was cross-linked with sodium benzoate under light irradiation (Figure S2). This layer can be arbitrarily patterned by using masks (see Figure S3 for arraying process); the middle layer is a compliant polydimethylsiloxane (PDMS) film; and the under layer is a transparent supporting substrate based on polyethylene terephthalate (PET), polymethyl methacrylate (PMMA) or glass. A ligand-free inorganic cesium lead halide (Cs-Pb-Br) perovskite was next introduced into the cross-linked PVA layer by swelling it with the precursor solution (Fig. 1a, middle), and the perovskite content was regulated by tuning the solution concentration (Figure S4). After subsequent drying and post-treatment, we obtained the desired composite film (Fig. 1a, right). Cross-sectional scanning electron microscope (SEM) images (Fig. 1b and Figure S5) and corresponding energy dispersive spectroscopy (EDS) results (Figure S6) of the as-prepared film show that perovskite nanoparticles (NPs) with sizes of 200–400 nm are evenly distributed in PVA (also see fluorescence micrograph in Figure S7 and transmission electron microscope images in Figure S8).

The prepared composite film is transparent under natural light and fluorescent under ultraviolet (UV) light (Fig. 1c, left). After wetting with an ultrasonic humidifier (Figure S9), the film becomes translucent and non-fluorescent (Fig. 1c, right). Meanwhile, the patterned film with arrays of circular disks (Fig. 1d, left and middle) showed a similar change of the fluorescence and transparency upon water spraying (Fig. 1d, right and Figure S10). In particular, photoluminescence (PL) spectroscopy showed that the emission peak of the film in the dry state locates at around 510 nm, with a full width at half maximum (FWHM) of about 20 nm. After wetting, the emission peak completely disappeared (Fig. 1e). This on/off switching of fluorescence is reversible and reproducible (see Video S1) with a consistent peak position and intensity for at least fifteen cycles (Fig. 2f). We also found that the transmittance of the film in the visible light range was above 90 % in the dry state and below 10 % in the wet state (Fig. 1g). This is caused by the wrinkle formation in the swollen PVA layer that can significantly scatter incident light⁴⁶ (bottom inset in Fig. 1g, and see the 3D microscope image in Figure S11). The changes in transmittances also demonstrated good reversibility and repeatability (see Video S2) in a fifteen-cycle study (Fig. 1h), as the PVA layer becomes flat again after de-swelling (top inset in Fig. 1g).

To understand the reversible fluorescence change, we conducted X-ray photoelectron spectroscopy (XPS) and X-ray diffraction (XRD) analysis of the composite film. In the dry (original) state. XPS results (Figure S12 and Table S1) show that the embedded perovskite has a stoichiometric composition of CsPb₂Br₅. The XRD study presents characteristic peaks at 11.7°, 23.4°, 35.4° and 47.8°, fitting well with the crystal planes (002), (210), (312) and (420) of the tetragonal CsPb₂Br₅ phase⁴⁷ (PDF#25–0211), respectively (Fig. 2a and Figure S13). These peaks disappeared after water treatment and recovered after drying

(Fig. 2a). We thus assume that perovskite NPs have dissociated into free ions (Cs^+ , Pb^{2+} , Br^- or PbBr_6^{4-}) that are dissolved in the swollen PVA network in the wet state, and the ions can recrystallize into NPs again after water evaporation (Fig. 2b). To verify this, electrical measurements on the same film sample were performed (Fig. 2c and Figure S14). The conductivity of the film indeed increases from $10^{-4} \text{ S}\cdot\text{m}^{-1}$ to $10^{-1} \text{ S}\cdot\text{m}^{-1}$ after wetting and reduces back to $10^{-4} \text{ S}\cdot\text{m}^{-1}$ after drying. The conductivity in the wet state is at least one order of magnitude higher than that of the reference sample containing no perovskite. These results further explain the fluorescence quenching in the wet state and subsequent recovery in the dry state.

The reversible dissociation and recrystallization of perovskite species above is highly intriguing in connection to fact that perovskites are highly susceptible to water molecules, *i.e.* water would usually induce irreversible dissociation of these ionic crystals, strongly affecting their opto-electric properties^{48–50}. Such a reversible ion-to-crystal transformation (RICT) can be attributed to the cross-linked PVA network. Further control experiments show that perovskite NPs cannot grow uniformly in PVA film without cross-linking (Figure S15). Likewise, their dissociation becomes irreversible without cross-linking. Notably, PVA hydrogels have been used as solar steam generators in seawater desalination for restricting ion diffusion while allowing water evaporation^{51,52}. Their networks can also be used as templates to regulate the growth of metal NPs such as Fe, Co, Ni, Cu, *etc.*^{53,54} Thus, we postulate that the PVA network serve as semi-enclosed “cages” (Fig. 2b) that not only absorb a sufficient amount of water to dissociate perovskite NPs but at the same time confines the migration of ions (Cs^+ , Pb^{2+} , Br^- or PbBr_6^{4-}) and subsequently nano-spatially nucleates their recrystallization for realizing RICT. It is worth noting that such RICT also works for a lead-free double perovskite $\text{Cs}_2\text{AgBiBr}_6$ (Figure S16), *i.e.*, its composite film also shows good reversibility and reproducibility of the fluorescence signal in at least four cycles (Figure S17).

We further studied the sequence of wrinkle formation and transformation of perovskite NPs and their eventual synergy during wetting. Our real-time monitoring of water spraying on the composite film shows that the transparency declined (1–2 s, Video S2) before the fluorescence quenching takes place (4–5 s, Video S1). This result suggests that water molecules first permeate and swell the PVA matrix to form wrinkles and subsequently react with the embedded perovskites NPs to dissolve them into the constituting ions. We further prepared different composite film with different amounts of perovskite (2.5–11.5 vol.%) with a fixed PVA layer thickness of 3.6 μm and measured the water absorption amount per unit area of these films. We found that the amount of water required to completely quench the fluorescence increases from 3.2 to 4.5 mg/cm^2 as function of increasing perovskite concentration, while the amount of water needed to form wrinkles remains almost constant at a value of $\sim 0.6 \text{ mg}/\text{cm}^2$ (Fig. 2d). These results confirm that water first triggers wrinkles and then quenches the fluorescence.

Interestingly, we could quantitatively evaluate the amount of water absorption based on the light scattering properties of the swollen films. In particular, we built a measuring setup by combining a camera and a precision balance to synchronously record the surface brightness (grayscale) and weight of a film sample in real time. (see details in “Methods” and Figure S18). We could thus obtain time-

varying curves of the average grayscale value and water absorption (Fig. 2e) and quantitatively establish their relation after normalization with a reference sample (Fig. 2f and Figure S19). For the film sample with PVA thickness of 1.8 μm (6 wt.% cross-linker), a linear dependency in the range of 0–0.3 mg/cm^2 can be observed, with good reproducibility in repeating runs, even at different illuminances (15 and 120 lux). Moreover, this linear response range can be precisely engineered by tuning the film thickness (Figure S20 and S21). Specifically, increasing the PVA layer thickness from 1.8 to 11.6 μm linearly increases the saturated absorption of water from 0.3 to 2.4 mg/cm^2 (Fig. 2g), respectively, approaching the fluorescent sensing range of bespoke perovskite NPs.

Based on the above results, we anticipate the prospect to regulate the water absorption capability (or sensing threshold) and linear response range of the composite films by tuning the perovskite content and PVA thickness, respectively. Notably, the on/off switching of fluorescence is expected not to interfere with the gradual change of transmittance or grayscale of the film, and these two responses can thus be manipulated independently as the fluorescence switching of perovskite requires a large amount of water qualitatively, while wrinkle formation is a gradual physical process sensitive to a lower amount of water. This markedly different response of the different constituents of the polymer composite will be critical for practical applications in sensing and other fields.

As a demonstration, we studied the application of the composite film as a sensor in the real-time detection of water spraying. Rapid, low-cost, and non-disposable detection of the amount and distribution of sprayed droplets at given locations, *e.g.*, on the leaves or in the field, is urgently needed in precision agriculture but yet to be realized. Currently, water sensitive paper (WSP) is widely used for the agricultural spray detection^{55–58}, which is neither reusable nor suited for real-time monitoring. Moreover, it follows a routine of “field sampling first and lab analysis later” that severely limits its application in today’s unmanned agricultural practices.

We first conducted a droplet impact experiment and found that our composite film with hydrophilic surface facilitates the droplet deposition with little rebounding or splashing (Figure S22). Ideally, we can obtain real-time spraying data by recording the distribution of grayscale values or fluorescence at different positions of the composite film. In practice, however, we found that water droplets could spread laterally on the surface layer and overlap with each other, resulting in a reduced spatial resolution (Fig. 3a, left). To address this issue, we used the patterned composite film containing arrays of circular disks ($\sim 300 \mu\text{m}$) with the assumption that the isolated cells can work independently to localize the diffusion of water (Fig. 1d). We found the arrayed film provided a much higher resolution of the droplet distribution under the same spraying conditions (Fig. 3a, right), *i.e.*, the response of the spots remained small in size and was almost free of lateral extension (also see Figure S23). We further took a series of micrographs from a typical spray-recovery process (Fig. 3b, also see Video S3). As expected, the hydrophobic PDMS patches in between cells prevents water from spreading, and the distribution of the wrinkled cells reflects the distribution of water droplets. We thus can obtain the distribution of the sprayed droplets by using the patterned film sensor.

Moreover, we found that the patterned structure also significantly improves the overall flexibility of the film, enabling it to be arbitrarily folded or twisted with little effect on its sensing capability (Fig. 3c and Figure S24). A bending test under a microscope showed that at the same bending radius of 2.5 mm (Figure S25), the continuous film without array presented unfavorable wrinkles and even cracks (Fig. 3d, left), while the curved film with arrays retained the original intact morphology (Fig. 3d, right). The arrays break the continuity of the surface layer, which reduces the shear stress transfer between layers during bending and thus minimizes mechanical strain and wrinkles^{59–62}. These results highlight the application potential of our composite film in wearable detection.

We next studied the sensing performance of our composite film in different application scenarios. We first demonstrated a bandage-like device that can be attached onto plant leaves (Fig. 4a). In particular, we peeled off the pre-prepared composite film (~ 5 vol.% perovskite in 3.6 μm PVA on PDMS, size ~ 1×1 cm) from its original substrate (glass) and transferred it to leaves of a plant (*Schefflera octophylla*, for example). The flexible film can be readily fitted to the leaf surface (Fig. 4b). Its fluorescence disappears after spraying and recovers after drying, ready for the next test (Fig. 4c). Therefore, we consider that the composite film can be used as a wearable sensor in practice, *i.e.*, by placing it at different positions of the crop (leaves, stems, fruits, *etc.*) for the on/off detection of spraying and its distribution. Notably, the response range of our composite film to water (0–4.5 mg/cm^2 , Fig. 2d) is consistent with the actual spraying densities of pesticides^{63,64} (e.g., insecticides, herbicides, fungicides, *etc.*) ranging from 0.5 to 3.0 mg/cm^2 (or 50–300 L/ha) in agriculture. Moreover, fluorescence-based detection, enabled by our composite film, can be performed under low ambient light or even at night.

We further designed a portable device (Fig. 4d) with the composite film sitting on the top of a sealed home-made box for spraying detection in the field. A micro-camera with Wi-Fi transmitter was installed at the bottom center of the box for monitoring the film and transmitting real-time signals wirelessly. A water spraying test with this device was first performed in a laboratory environment, acquiring the result of one spray-recovery circle (Fig. 4e and Figure S26), where the white spots were attributed to the local wrinkles triggered by water droplets. After the test, our device could recover spontaneously and be reused. We further performed an outdoor test in a field environment under natural, ambient light (Figure S27) and obtained results after background subtracting (Fig. 4f). A database of droplets could be established based on image recognition, and we could thus statistically analyze and acquire the desired spraying information quantitatively including the number of droplets (N), their average size (s), the average spacing between droplets (d), the total water volume (V), and the coverage ratio (C) (see the analysis and a typical list of results in Figure S28). Moreover, because the sensor devices are portable and recoverable, they can be placed at different positions (p_1, p_2, \dots, p_n) and record a series of data at different moments (t_1, t_2, \dots, t_n), respectively. All these data obtained from our composite film sensors are acquired in real time, and thus they can provide timely feedback and guidance on field operations, *e.g.* spraying operation by unmanned aerial vehicle (UAV). In this way, we can achieve precise spraying control of pesticides in an automated and intelligent manner for precision agriculture (Fig. 4g).

In summary, we have developed reconfigurable polymer composites presenting water-switchable transmittance and fluorescence with good reversibility and independent controllability. The top hydratable layer of the composite can form surface wrinkles reversibly, triggered by water, while perovskites inside the layer undergo reversible ion-to-crystal transformations because of nanoconfinement in the voids of the crosslinked hydrogel. The two responses can work cooperatively, permitting an unrivaled sensing application of the composite film in precision agriculture, *i.e.*, a rapid and reusable on-site detection of water spraying in terms of quantity, threshold, and distribution. Our findings suggest that multiple functionalities can emerge from the hierarchical interactions between the multiscale constituents, which would give access to perovskite-based smart composites and flexible devices with novel applications.

Declarations

Acknowledgements

We thank Y. H. Yang and Z. Y. Zhang for SEM measurements, C. Zhang for TEM measurements, J. G. Du for electrical measurements, and J. J. Wu and H. Pan for the spraying tests. This work was supported by National Natural Science Foundation of China (Grant No. 22078276 & 22005260), the Program for Guangdong Introducing Innovative and Entrepreneurial Teams (Grant No. 2017ZT07C291), Shenzhen Science and Technology Program (Grant No. KQTD20170810141424366), Shenzhen Key Laboratory of Advanced Materials Product Engineering (Grant No. ZDSYS20190911164401990). This work was also supported by the National Natural Science Foundation of China (Grants 22078289, 22078282, 21938010, 51903218, and 2197080461), Zhejiang Provincial Natural Science Foundation of China under Grant No. LR20B060002, the Chinese State Key Laboratory of Chemical Engineering at Zhejiang University (Grants SKL-ChE-20T04, SKL-ChE-19T03). H. Z. thanks the China Postdoctoral Science Foundation (Grant No. 2018M642537) and Q. Z. thanks the Presidential Fund (Grant No. PF01000949) for supporting their research at CUHK-Shenzhen. J.H. acknowledges financial support from the Research Foundation-Flanders (FWO, Grant No. G098319N, G0A5817N, and ZW15_09-G0H6316N) and the Flemish government through long-term structural funding Methusalem (CASAS2, Meth/15/04)

References

1. McEvoy, M. A. & Correll, N. Materials science. Materials that couple sensing, actuation, computation, and communication. *Science* **347**, 1261689, doi:10.1126/science.1261689 (2015).
2. Ilami, M., Bagheri, H., Ahmed, R., Skowronek, E. O. & Marvi, H. Materials, Actuators, and Sensors for Soft Bioinspired Robots. *Adv Mater*, e2003139, doi:10.1002/adma.202003139 (2020).
3. Pang, C. *et al.* A flexible and highly sensitive strain-gauge sensor using reversible interlocking of nanofibres. *Nat Mater* **11**, 795–801, doi:10.1038/nmat3380 (2012).
4. Miriyev, A., Stack, K. & Lipson, H. Soft material for soft actuators. *Nat Commun* **8**, 596, doi:10.1038/s41467-017-00685-3 (2017).

5. Kim, Y. S. *et al.* Thermo-responsive actuation enabled by permittivity switching in an electrostatically anisotropic hydrogel. *Nat Mater* **14**, 1002–1007, doi:10.1038/nmat4363 (2015).
6. Wang, C., Wang, C., Huang, Z. & Xu, S. Materials and Structures toward Soft Electronics. *Adv Mater* **30**, e1801368, doi:10.1002/adma.201801368 (2018).
7. Ohm, Y. *et al.* An electrically conductive silver–polyacrylamide–alginate hydrogel composite for soft electronics. *Nature Electronics*, doi:10.1038/s41928-021-00545-5 (2021).
8. Jing, L., Li, K., Yang, H. & Chen, P.-Y. Recent advances in integration of 2D materials with soft matter for multifunctional robotic materials. *Materials Horizons* **7**, 54–70, doi:10.1039/c9mh01139k (2020).
9. Shen, Z., Chen, F., Zhu, X., Yong, K. T. & Gu, G. Stimuli-responsive functional materials for soft robotics. *J Mater Chem B*, doi:10.1039/d0tb01585g (2020).
10. Pena-Francesch, A., Jung, H., Demirel, M. C. & Sitti, M. Biosynthetic self-healing materials for soft machines. *Nat Mater* **19**, 1230–1235, doi:10.1038/s41563-020-0736-2 (2020).
11. Chen, L. *et al.* Multi-responsive actuators based on a graphene oxide composite: intelligent robot and bioinspired applications. *Nanoscale* **9**, 9825–9833, doi:10.1039/c7nr01913k (2017).
12. Zhang, X. *et al.* Optically- and thermally-responsive programmable materials based on carbon nanotube-hydrogel polymer composites. *Nano Lett* **11**, 3239–3244, doi:10.1021/nl201503e (2011).
13. Alam, A., Zhang, Y., Kuan, H.-C., Lee, S.-H. & Ma, J. Polymer composite hydrogels containing carbon nanomaterials—Morphology and mechanical and functional performance. *Progress in Polymer Science* **77**, 1–18, doi:10.1016/j.progpolymsci.2017.09.001 (2018).
14. Jo, C., Pugal, D., Oh, I.-K., Kim, K. J. & Asaka, K. Recent advances in ionic polymer–metal composite actuators and their modeling and applications. *Progress in Polymer Science* **38**, 1037–1066, doi:10.1016/j.progpolymsci.2013.04.003 (2013).
15. Jiang, C., Markutsya, S., Pikus, Y. & Tsukruk, V. V. Freely suspended nanocomposite membranes as highly sensitive sensors. *Nat Mater* **3**, 721–728, doi:10.1038/nmat1212 (2004).
16. Kabra, D., Song, M. H., Wenger, B., Friend, R. H. & Snaith, H. J. High Efficiency Composite Metal Oxide-Polymer Electroluminescent Devices: A Morphological and Material Based Investigation. *Advanced Materials* **20**, 3447–3452, doi:10.1002/adma.200800202 (2008).
17. Style, R. W., Tutika, R., Kim, J. Y. & Bartlett, M. D. Solid–Liquid Composites for Soft Multifunctional Materials. *Advanced Functional Materials* **31**, doi:10.1002/adfm.202005804 (2020).
18. Srivastava, S., Schaefer, J. L., Yang, Z., Tu, Z. & Archer, L. A. 25th anniversary article: polymer-particle composites: phase stability and applications in electrochemical energy storage. *Adv Mater* **26**, 201–234, doi:10.1002/adma.201303070 (2014).
19. Zhang, Z. *et al.* Polymer nanocomposites with aligned two-dimensional materials. *Progress in Polymer Science* **114**, doi:10.1016/j.progpolymsci.2021.101360 (2021).
20. Stuart, M. A. *et al.* Emerging applications of stimuli-responsive polymer materials. *Nat Mater* **9**, 101–113, doi:10.1038/nmat2614 (2010).

21. Chen, H., Yang, F., Chen, Q. & Zheng, J. A Novel Design of Multi-Mechanoresponsive and Mechanically Strong Hydrogels. *Adv Mater* **29**, doi:10.1002/adma.201606900 (2017).
22. Li, P., Zhang, J. & Dong, C.-M. Photosensitive poly(o-nitrobenzyloxycarbonyl-L-lysine)-b-PEO polypeptide copolymers: synthesis, multiple self-assembly behaviors, and the photo/pH-thermo-sensitive hydrogels. *Polymer Chemistry* **8**, 7033–7043, doi:10.1039/c7py01574g (2017).
23. Yue, Y. *et al.* Mechano-actuated ultrafast full-colour switching in layered photonic hydrogels. *Nat Commun* **5**, 4659, doi:10.1038/ncomms5659 (2014).
24. Hou, H., Yin, J. & Jiang, X. Smart Patterned Surface with Dynamic Wrinkles. *Acc Chem Res* **52**, 1025–1035, doi:10.1021/acs.accounts.8b00623 (2019).
25. Zhang, Y. S. & Khademhosseini, A. Advances in engineering hydrogels. *Science* **356**, doi:10.1126/science.aaf3627 (2017).
26. Snaith, H. J. Present status and future prospects of perovskite photovoltaics. *Nat Mater* **17**, 372–376, doi:10.1038/s41563-018-0071-z (2018).
27. Park, N.-G. Perovskite solar cells: an emerging photovoltaic technology. *Materials Today* **18**, 65–72, doi:10.1016/j.mattod.2014.07.007 (2015).
28. Zhao, X., Ng, J. D. A., Friend, R. H. & Tan, Z.-K. Opportunities and Challenges in Perovskite Light-Emitting Devices. *ACS Photonics* **5**, 3866–3875, doi:10.1021/acsphotonics.8b00745 (2018).
29. Kim, Y.-H. *et al.* Comprehensive defect suppression in perovskite nanocrystals for high-efficiency light-emitting diodes. *Nature Photonics* **15**, 148–155, doi:10.1038/s41566-020-00732-4 (2021).
30. Song, J. *et al.* Quantum Dot Light-Emitting Diodes Based on Inorganic Perovskite Cesium Lead Halides (CsPbX₃). *Adv Mater* **27**, 7162–7167, doi:10.1002/adma.201502567 (2015).
31. Dey, A. *et al.* State of the Art and Prospects for Halide Perovskite Nanocrystals. *ACS Nano*, doi:10.1021/acsnano.0c08903 (2021).
32. Zhou, Q. *et al.* In Situ Fabrication of Halide Perovskite Nanocrystal-Embedded Polymer Composite Films with Enhanced Photoluminescence for Display Backlights. *Adv Mater* **28**, 9163–9168, doi:10.1002/adma.201602651 (2016).
33. Dou, L. *et al.* Solution-processed hybrid perovskite photodetectors with high detectivity. *Nat Commun* **5**, 5404, doi:10.1038/ncomms6404 (2014).
34. Ren, K. *et al.* Turning a disadvantage into an advantage: synthesizing high-quality organometallic halide perovskite nanosheet arrays for humidity sensors. *Journal of Materials Chemistry C* **5**, 2504–2508, doi:10.1039/c6tc05165k (2017).
35. Zhang, Y. *et al.* Robust and Swiftly Reversible Thermochromic Behavior of a 2D Perovskite of (C₆H₄(CH₂NH₃)₂)(CH₃NH₃)[Pb₂I₇] for Smart Window and Photovoltaic Smart Window Applications. *ACS Appl Mater Interfaces*, doi:10.1021/acsaami.1c00163 (2021).
36. Xu, W. *et al.* An ultrasensitive and reversible fluorescence sensor of humidity using perovskite CH₃NH₃PbBr₃. *Journal of Materials Chemistry C* **4**, 9651–9655, doi:10.1039/c6tc01075j (2016).

37. Zhou, Y. & Zhao, Y. Chemical stability and instability of inorganic halide perovskites. *Energy & Environmental Science* **12**, 1495–1511, doi:10.1039/c8ee03559h (2019).
38. Aranda, C., Guerrero, A. & Bisquert, J. Crystalline Clear or Not: Beneficial and Harmful Effects of Water in Perovskite Solar Cells. *Chemphyschem* **20**, 2587–2599, doi:10.1002/cphc.201900393 (2019).
39. Di Girolamo, D. *et al.* Dual effect of humidity on cesium lead bromide: enhancement and degradation of perovskite films. *Journal of Materials Chemistry A* **7**, 12292–12302, doi:10.1039/c9ta00715f (2019).
40. Huang, J., Tan, S., Lund, P. D. & Zhou, H. Impact of H₂O on organic–inorganic hybrid perovskite solar cells. *Energy & Environmental Science* **10**, 2284–2311, doi:10.1039/c7ee01674c (2017).
41. Guo, X. *et al.* Cesium Oleate Passivation for Stable Perovskite Photovoltaics. *ACS Appl Mater Interfaces* **11**, 27882–27889, doi:10.1021/acsami.9b08026 (2019).
42. Hwang, I., Jeong, I., Lee, J., Ko, M. J. & Yong, K. Enhancing Stability of Perovskite Solar Cells to Moisture by the Facile Hydrophobic Passivation. *ACS Appl Mater Interfaces* **7**, 17330–17336, doi:10.1021/acsami.5b04490 (2015).
43. Zhang, Y. *et al.* Homogeneous Freestanding Luminescent Perovskite Organogel with Superior Water Stability. *Adv Mater* **31**, e1902928, doi:10.1002/adma.201902928 (2019).
44. Wang, Y. *et al.* Ultrastable, Highly Luminescent Organic-Inorganic Perovskite-Polymer Composite Films. *Adv Mater* **28**, 10710–10717, doi:10.1002/adma.201603964 (2016).
45. Ko, J., Ma, K., Joung, J. F., Park, S. & Bang, J. Ligand-Assisted Direct Photolithography of Perovskite Nanocrystals Encapsulated with Multifunctional Polymer Ligands for Stable, Full-Colored, High-Resolution Displays. *Nano Lett* **21**, 2288–2295, doi:10.1021/acs.nanolett.1c00134 (2021).
46. Zeng, S. *et al.* Moisture-Responsive Wrinkling Surfaces with Tunable Dynamics. *Adv Mater* **29**, doi:10.1002/adma.201700828 (2017).
47. Qin, C., Matsushima, T., Sandanayaka, A. S. D., Tsuchiya, Y. & Adachi, C. Centrifugal-Coated Quasi-Two-Dimensional Perovskite CsPb₂Br₅ Films for Efficient and Stable Light-Emitting Diodes. *J Phys Chem Lett* **8**, 5415–5421, doi:10.1021/acs.jpcllett.7b02371 (2017).
48. Ouyang, Y., Shi, L., Li, Q. & Wang, J. Role of Water and Defects in Photo-Oxidative Degradation of Methylammonium Lead Iodide Perovskite. *Small Methods* **3**, doi:10.1002/smt.201900154 (2019).
49. Chun-Ren Ke, J. *et al.* In situ investigation of degradation at organometal halide perovskite surfaces by X-ray photoelectron spectroscopy at realistic water vapour pressure. *Chem Commun (Camb)* **53**, 5231–5234, doi:10.1039/c7cc01538k (2017).
50. Kye, Y. H., Yu, C. J., Jong, U. G., Chen, Y. & Walsh, A. Critical Role of Water in Defect Aggregation and Chemical Degradation of Perovskite Solar Cells. *J Phys Chem Lett* **9**, 2196–2201, doi:10.1021/acs.jpcllett.8b00406 (2018).
51. Zhou, X., Guo, Y., Zhao, F. & Yu, G. Hydrogels as an Emerging Material Platform for Solar Water Purification. *Acc Chem Res* **52**, 3244–3253, doi:10.1021/acs.accounts.9b00455 (2019).

52. Zhou, X., Zhao, F., Guo, Y., Zhang, Y. & Yu, G. A hydrogel-based antifouling solar evaporator for highly efficient water desalination. *Energy & Environmental Science* **11**, 1985–1992, doi:10.1039/c8ee00567b (2018).
53. Sahiner, N. Soft and flexible hydrogel templates of different sizes and various functionalities for metal nanoparticle preparation and their use in catalysis. *Progress in Polymer Science* **38**, 1329–1356, doi:10.1016/j.progpolymsci.2013.06.004 (2013).
54. Sahiner, N. In situ metal particle preparation in cross-linked poly(2-acrylamido-2-methyl-1-propansulfonic acid) hydrogel networks. *Colloid and Polymer Science* **285**, 283–292, doi:10.1007/s00396-006-1562-z (2006).
55. Sanchez-Hermosilla, J. & Medina, R. Adaptive threshold for droplet spot analysis using water-sensitive paper. *Appl Eng Agric* **20**, 547–551 (2004).
56. Nishida, K., Ishii, M., Tsushima, S. & Hirai, S. Detection of water vapor in cathode gas diffusion layer of polymer electrolyte fuel cell using water sensitive paper. *J Power Sources* **199**, 155–160, doi:10.1016/j.jpowsour.2011.10.026 (2012).
57. Zhu, H., Salyani, M. & Fox, R. D. A portable scanning system for evaluation of spray deposit distribution. *Comput Electron Agr* **76**, 38–43, doi:10.1016/j.compag.2011.01.003 (2011).
58. Otto, S. *et al.* Droplets deposition pattern from a prototype of a fixed spraying system in a sloping vineyard. *Sci Total Environ* **639**, 92–99, doi:10.1016/j.scitotenv.2018.05.167 (2018).
59. Wang, S., Huang, Y. & Rogers, J. A. Mechanical Designs for Inorganic Stretchable Circuits in Soft Electronics. *IEEE Trans Compon Packaging Manuf Technol* **5**, 1201–1218, doi:10.1109/TCPMT.2015.2417801 (2015).
60. Bowen, J. J., Taylor, J. M., Jurich, C. P. & Morin, S. A. Stretchable Chemical Patterns for the Assembly and Manipulation of Arrays of Microdroplets with Lensing and Micromixing Functionality. *Advanced Functional Materials* **25**, 5520–5528, doi:10.1002/adfm.201502174 (2015).
61. Kim, T., Lee, H., Jo, W., Kim, T. S. & Yoo, S. Realizing Stretchable OLEDs: A Hybrid Platform Based on Rigid Island Arrays on a Stress-Relieving Bilayer Structure. *Advanced Materials Technologies* **5**, doi:10.1002/admt.202000494 (2020).
62. Wang, S. *et al.* Skin electronics from scalable fabrication of an intrinsically stretchable transistor array. *Nature* **555**, 83–88, doi:10.1038/nature25494 (2018).
63. Castoldi, J. P. T. *et al.* Pesticide Application Quality With Alternative Use of Water Sensitive Paper. *Journal of Agricultural Science* **11**, doi:10.5539/jas.v11n6p528 (2019).
64. Wolf, R. E. Assessing the ability of DropletScan (TM) to analyze spray droplets from a ground operated sprayer. *Appl Eng Agric* **19**, 525–530 (2003).

Figures

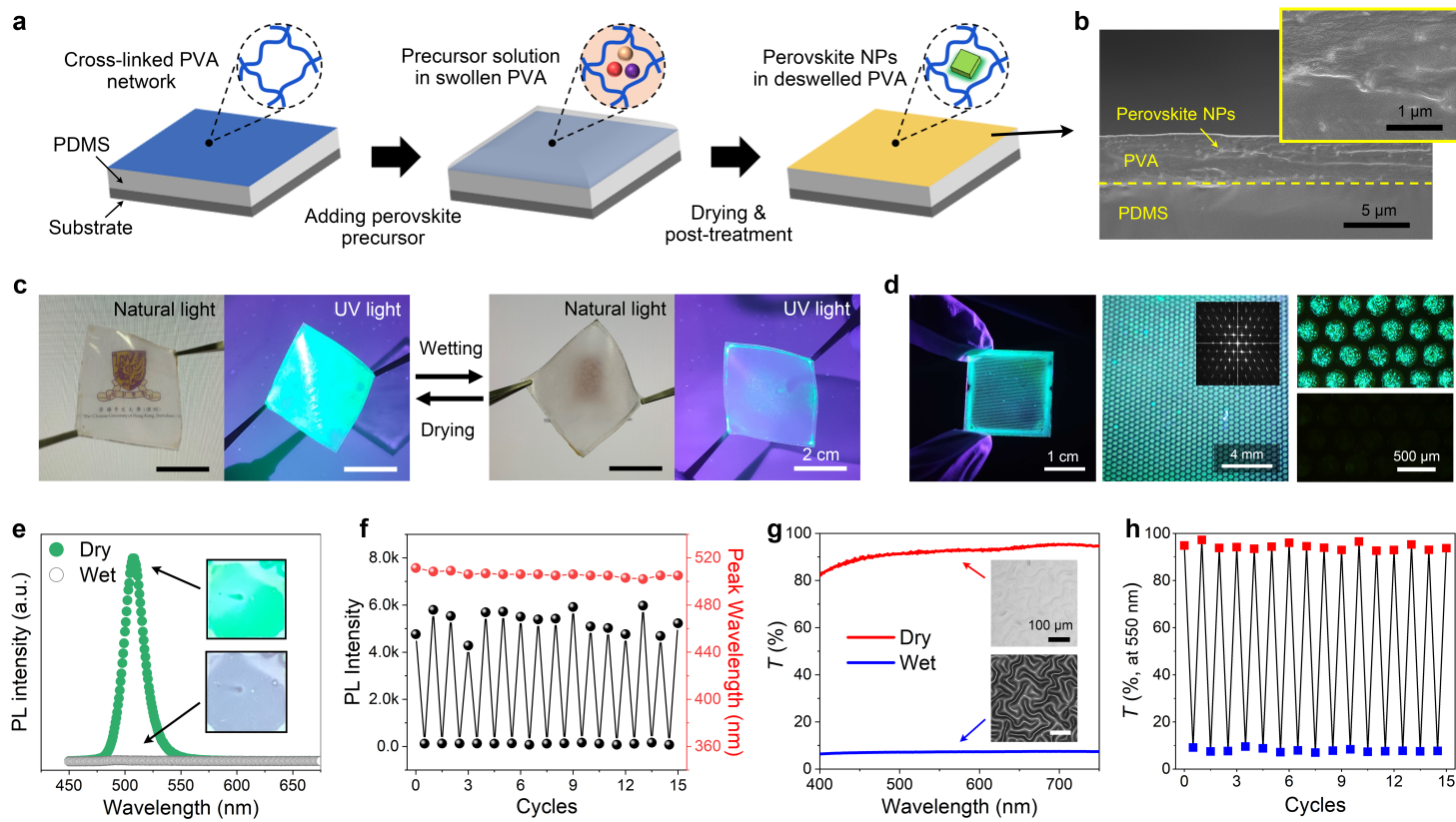


Figure 1

(a) Schematic diagram of the fabrication process of the composite film. (b) Cross-sectional SEM images of the composite film. (c) Experimental results of the composite film with reversible change with water spray and recovery in both natural and UV light. (d) Arrayed composite film under UV light and its micro-fluorescence change after water spraying and recovery. (e) PL spectra of the imbedded perovskite NPs in dry and wet states. (f) The change of PL intensity and peak position during 15 cycles. (g) Transmission spectrum curves in visible light range of the multi-layer film in flat and wrinkled states. (h) Transmittance at 550 nm of the multi-layer film for 15 cycles between flat and wrinkled states.

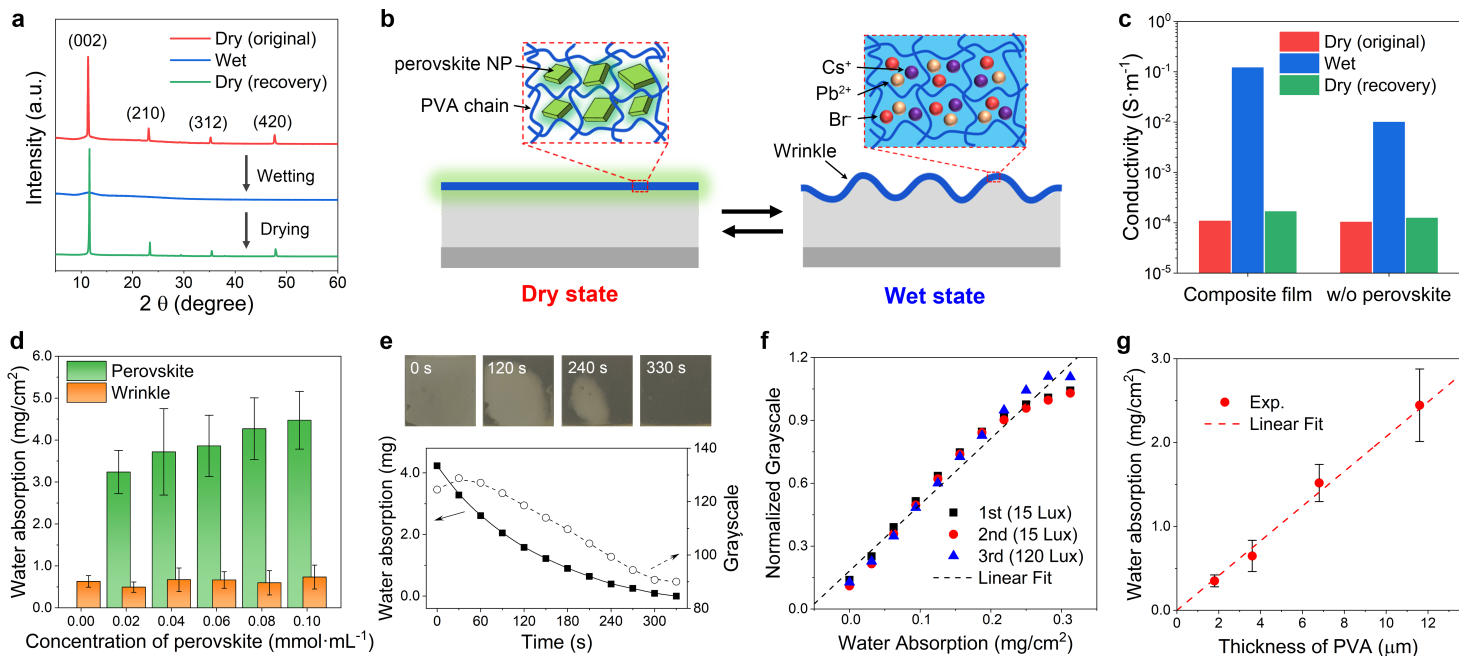


Figure 2

(a) XRD results of the composite film after one wetting-drying circle. (b) Schematic diagram of the composite film with reversible changes, including the surface light-scattering wrinkle structure and fluorescent perovskite NPs. (c) Conductivities of the composite film and the film without perovskite at one wetting-drying circle. (d) Water absorption threshold amounts for perovskite (green) and wrinkle (orange) of the composite films by using different concentration of perovskite precursor solution. (e) Top: Images of the evolution of the surface of the multi-layer film from a wet/wrinkled state to a completely dry/flat state. Bottom: Curves of water absorption and grayscale value along with time. (f) Plots of normalized grayscale value versus water absorption at different ambient illuminances. (g) Linear relation between the water absorption amount and the thickness of PVA layer.

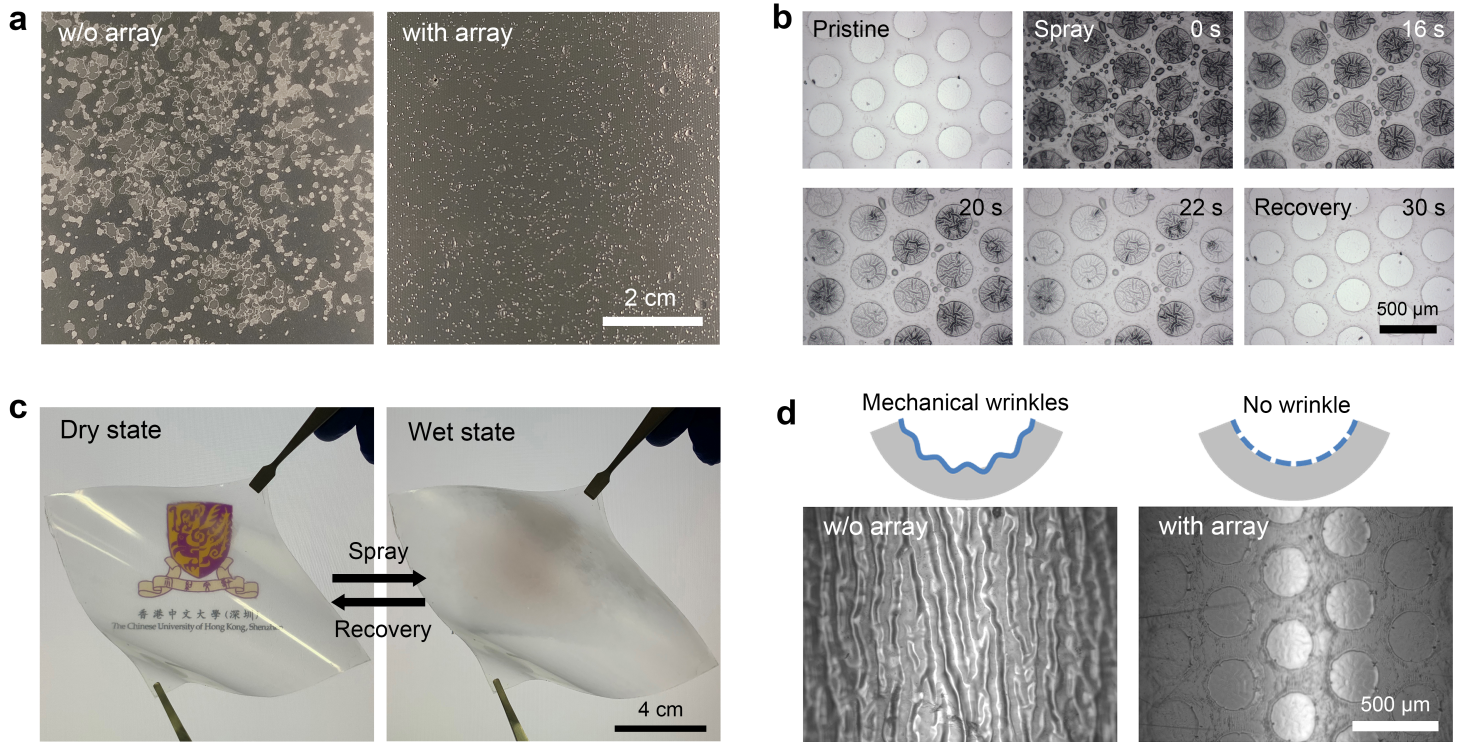


Figure 3

(a) Experimental spray results on the film with and without array. (b) Morphologic evolution of the wrinkles on the arrayed multi-layer film after spraying with water and subsequent recovery. (c) Macroscopic photographs of droplet spraying on the flexible films. (d) Schematic diagram and experimental results of the arrayed and continuous film upon bending in dry state.

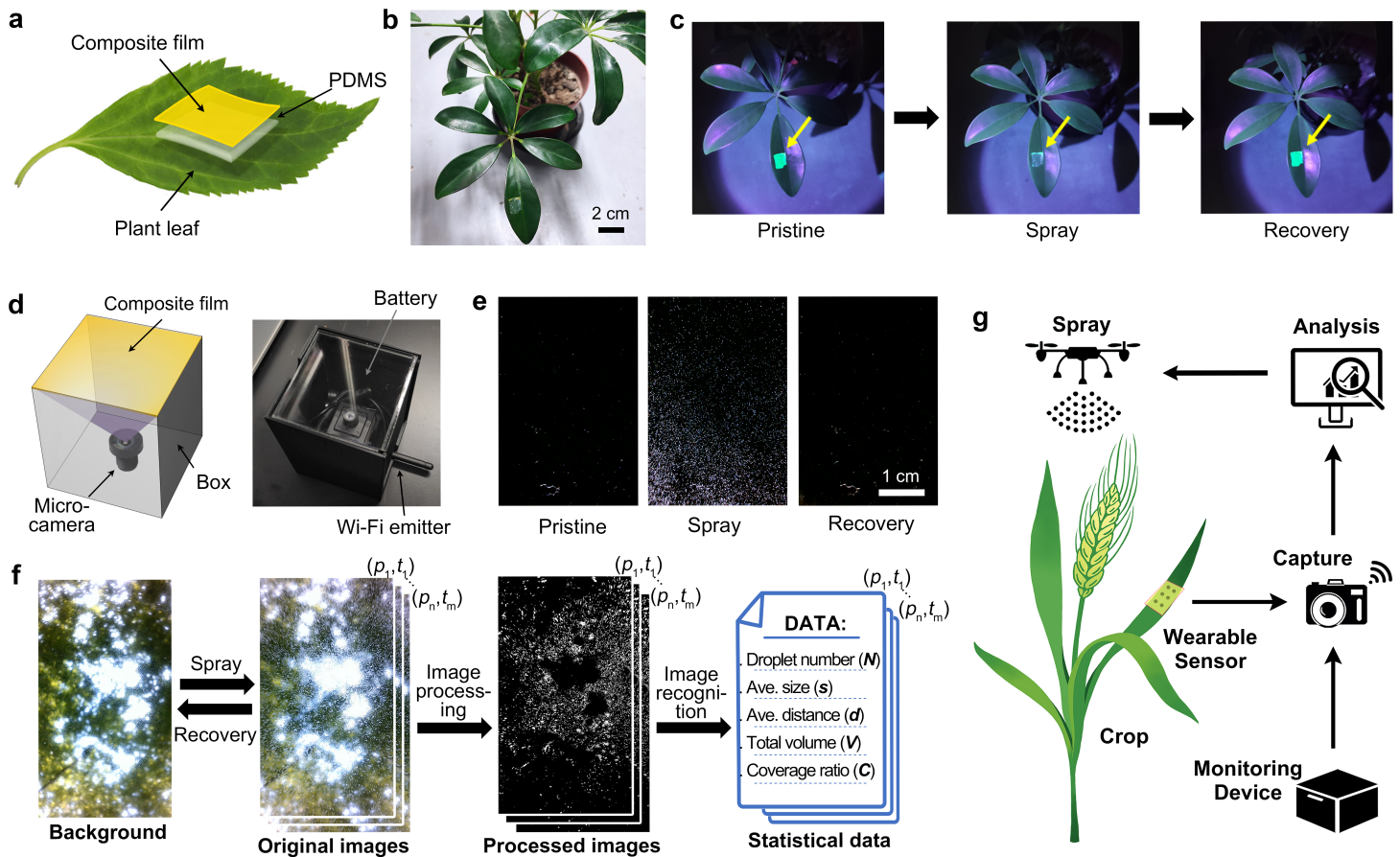


Figure 4

(a) Schematic diagram the wearable sensor attached on a plant leaf. (b) Photographs of an experimental spray test on a *Schefflera octophylla* leaf. (c) Experimental results of the wearable sensor under spray and recovery. (d) Schematic diagram and the corresponding prototype of the box-type sensor with built-in micro-camera, battery and Wi-Fi emitter. (e) Experimental results of a typical test of water drop spray. (f) Flow chart of data acquisition and processing in practical outdoor test. (g) Schematic diagram of wearable sensor and monitoring device used in precision agriculture to guide pesticide spraying of unmanned aerial vehicle (UAV).

Supplementary Files

This is a list of supplementary files associated with this preprint. Click to download.

- [VideoS3.mp4](#)
- [VideoS1.mp4](#)
- [VideoS2.mp4](#)
- [Supportinformation.docx](#)